Image Thresholding by Indicator Kriging

Wonho Oh and W. Brent Lindquist

Abstract—We consider the problem of segmenting a digitized image consisting of two univariate populations. Assume a priori knowledge allows incomplete assignment of voxels in the image, in the sense that a fraction of the voxels can be identified as belonging to population Π_0, a second fraction to Π_1, and the remaining fraction have no a priori identification. Based upon estimates of the short length scale spatial covariance of the image, we develop a method utilizing indicator kriging to complete the image segmentation.

Index Terms—Image segmentation, spatial thresholding, indicator kriging.

1 Introduction

We are interested in the problem of image segmentation by thresholding for the two population univariate case when an image consists of an object (population Π_1), of possibly complicated shape, and a background (population Π_0). Our work is motivated by three dimensional synchrotron X-ray computed tomographic (CAT) or laser scanning confocal microscopic (LSCM) images of biphase materials, such as rock samples, which for our purposes consist of a material (object) and a void (background) phase. Identifying the shape of the object is complicated by the partial voxel (finite volume of resolution) effect as well as by other noise due to tomographic reconstruction or data taking.

It is still common practice to use global thresholding to segment such images, often choosing the threshold value to enforce a bulk measurement of the porosity (volume fraction of the void phase). Such thresholding produces misclassification errors proportional to the percentage of overlapping values common to the two univariate populations. There is also the possibility that the bulk porosity measurement is in disagreement with the porosity of the imaged subvolume.

The problem of image segmentation is widely studied in character recognition, range imaging, medical imaging, and remote sensing, with numerous approaches developed to reduce misclassification errors from that produced by naive thresholding. Pal and Pal [1] review various methods for segmenting gray-scale images. Methods reviewed include thresholding, iterative pixel classification based on relaxation, Markov random field or neural network based methods, edge detection, and a method based on fuzzy set theory. We also note the approach developed by Tek and Kimia [2] which uses a shock-based morphogenetic language where the growth of four types of shocks results in a description of shape. More recently, several thresholding methods have been evaluated by Ø.D. Trier and A.K. Jain [3].

• *Both authors are with the Department of Applied Mathematics and Statistics, State University of New York at Stony Brook, Stony Brook, NY 11794-3600. E-mail: {linquis, woh}@ams.sunysb.edu.*

Manuscript received 28 May 1998; revised 22 Mar. 1999.
Recommended for acceptance by M. Shah.
For information on obtaining reprints of this article, please send e-mail to: tpami@computer.org, and reference IEEECS Log Number 107681.

The method introduced in this paper can be classified as a thresholding scheme. Image thresholding can be handled globally, determining a single threshold for the entire image, or locally, applying different thresholds in different spatial regions. In either case, thresholding methods break into two classes according to whether spatial information is incorporated in the segmentation. By utilizing information on higher moments, methods that incorporate spatial dependence information offer the promise of greater segmentation accuracy.

Examples of global thresholding methods that rely on gray-level information and ignore spatial dependence include those based upon maximization of an entropy function [4], [5], [6], [7], maximization of class separability [8], (the familiar K-means clustering algorithm [9] which maximizes separability utilizing distance measure in gray scale or color space also falls in this category), and minimization of misclassification error [10], [11], [12]. As an example that utilizes spatial information, the method by O'Gorman [13] chooses that global threshold which best preserves the connectivity of regions within the image. The global thresholding methods of [14], [15], [16] incorporate spatial information by means of a co-occurrence matrix. Spatial constraints have been applied to the K-means method using Gibbs random fields [17].

Examples of local thresholding methods that rely only on gray-level information include the following. A threshold can be determined for each voxel in the image, either by utilizing the local mean and variance [18], the local contrast [19], or by a biased running average [20]. The image can be partitioned into several nonoverlapping blocks and a threshold for each block computed independently, for example by a bimodal fit [21], [22]. Spatial discontinuity in the local threshold value can be avoided by interpolation over the entire image to yield a smooth threshold surface [11], [23].

To incorporate spatial information in local thresholding, Yanowitz and Bruckstein [24] utilize edge information. Edges are detected as local maxima in the image gradient. The gray level of the edge pixels are used as local thresholds. The local thresholds are then interpolated to obtain a threshold surface. In contrast, Mardia and Hainsworth [25] developed a general class of methods which use

local spatial information in terms of the two point covariance function for the image.

In this paper, we present a thresholding method that utilizes the spatial covariance of the image in conjunction with indicator kriging to determine object edges. Use of indicator kriging makes the thresholding local and guarantees smoothness in the threshold surface. Implementation of the method requires a priori population identification of some percentage of the image. In practice, this is not difficult to achieve. For example, based upon the gray-level histogram, it is often possible to identify the population type of much of the image (e.g., those voxels lying interior to objects in the image) with negligible identification error. The majority of the identification problem comes from object-edge voxels. Thus, a first pass over the image produces population assignments for a fraction of the (in general, nonedge) voxels, leaving a remaining fraction unidentified. We then utilize minimum variance estimation (kriging) to complete the segmentation of the image.

In appearance, our method has similarities to the general class of spatial thresholding algorithms developed by Mardia and Hainsworth [25]. However the Mardia-Hainsworth (MH) method relies on the maximization of a score function which is parameterized by the unknown means, standard deviations, and correlation functions of the populations in the image. Additionally, the score function is based upon an underlying assumption of Gaussian statistics. If prior information of these parameters is available, the MH algorithm is single-pass; if prior information is unavailable, an iterative method [26] is used until a self-consistent solution is obtained.

Our algorithm, based upon indicator kriging, is a nonparametric formulation, requiring only the estimation of the spatial covariance function for an indicator variable. In practice, information of the covariance function only over a limited range of short length scales is required.

In Section 2, we briefly review the concepts of ordinary and indicator kriging. In Section 3, we also briefly review the MH method to show the similarity in appearance with our algorithm. In Section 4, we develop the details of our indicator kriging method. In Section 5, we present results of kriging based segmentation for synthetic images and for CAT and LSCM images of rock samples and compare our results against the MH method, AMT-MF [25].

2 Indicator Kriging

Consider an unknown value $z(x_0)$ at the spatial location x_0 interpreted as an outcome of a random variable (RV) $Z(x_0)$. The n data values $z(x_\alpha), \alpha = 1, \ldots, n$ are likewise interpreted as n outcomes of n RVs $Z(x_\alpha)$. We assume that the $n+1$ RVs are related to the same attribute (e.g., x-ray attenuation coefficient in CAT images, fluorescence intensity in LSCM images) and are characterized by their common (unknown) mean

$$E\{Z(x_\alpha)\} = m, \quad \alpha = 1, \ldots, n, \tag{1}$$

and stationary spatial covariance

$$Cov\{Z(x_\alpha), Z(x_\beta)\} = C(x_\alpha - x_\beta). \tag{2}$$

A very readable introduction to kriging can be found in [27]. The basic idea is to produce an estimate

$$Z^*(x_0) \equiv \lambda_0 + \sum_{\alpha=1}^{n} \lambda_\alpha Z(x_\alpha) \tag{3}$$

of the unknown RV $Z(x_0)$ by linear regression, i.e., by a linear combination of the known RVs $Z(x_\alpha)$ plus a possible shift λ_0. Unlike classical regression, the data values are not "independent," but have correlation given by (2). The $n+1$ parameters $\lambda_i,\ i = 0, \ldots n$ are chosen to ensure $Z^*(x_0)$ is a good estimator of $Z(x_0)$. The usual choice is to require that Z^* be an unbiased estimator (i.e., the expected value of the error RV, $Z(x_0) - Z^*(x_0)$, be zero) and that the variance of the error RV be minimized, regardless of the value of the unknown mean m. This leads to a constrained minimization problem; the unknown λ values are given by the following "constrained normal" system of linear equations, also known as the ordinary kriging system

$$\begin{cases} \sum\limits_{\beta=1}^{n} \lambda_\beta C(x_\alpha - x_\beta) + \mu = C(x_\alpha - x_0), \quad \alpha = 1, \ldots, n, \\ \sum\limits_{\beta=1}^{n} \lambda_\beta = 1, \\ \lambda_0 = 0, \end{cases} \tag{4}$$

where μ is a Lagrange multiplier introduced to ensure the constraint. If the spatial covariance (2) is positive definite, the solution to (4) is unique.

Ordinary kriging has the exactitude property that if the unknown value position x_0 is taken to be one of the known data positions, say $x_{\alpha'}$, then the values of λ_α from the solution of (4) applied to (3) give $Z^*(x_0) = Z(x_{\alpha'})$. Thus, the surface $Z^*(x_0)$ honors the data values at data locations.

Ordinary kriging provides an "optimal" (as defined) value estimate at the location x_0 and provides as well an error variance for the estimate. However, in the image segmentation problem, a model which provides an estimated value at a location is less useful than a model which provides the probability that an unknown at an unsampled location is greater than a given threshold value. Indicator kriging provides this capability, capitalizing on the proportion of neighboring data valued above the same threshold, and accounting for the proximity of each datum to the unsampled location.

Define the indicator variables

$$i(z_c; x_\alpha) \equiv \begin{cases} 1, & \text{if } z(x_\alpha) \le z_c, \\ 0, & \text{otherwise.} \end{cases} \tag{5}$$

A linear estimate of the conditional probability that $z(x_0)$ is not greater than a given threshold z_c is given [28] by

$$\begin{aligned} P(z_c; x_0|n) &\equiv Prob\{z(x_0) \le z_c|n\} \\ &= \sum_{\alpha=1}^{n} \lambda_\alpha(z_c; x_0) i(z_c; x_\alpha) \end{aligned} \tag{6}$$

with $\lambda_\alpha(z_c; x_0) \ge 0$. Denoting the covariance of the indicator values $i(z_c; x_\alpha)$ by $C_I(z_c; h)$, the weights $\lambda_\alpha(z_c; x_0)$ are given [28] by the ordinary kriging system

$$\begin{cases} \sum_{\beta=1}^{n} \lambda_\beta(z_c; x_0) C_I(z_c; x_\alpha - x_\beta) + \mu(z_c; x_0) \\ \qquad = C_I(z_c; x_\alpha - x_0), \quad \alpha = 1, \ldots, n, \\ \sum_{\beta=1}^{n} \lambda_\beta(z_c; x_0) = 1. \end{cases} \tag{7}$$

Negative weights in the solution of (7) have the potential of producing negative probabilities in (6). If negative weights occur, we adjust the weights using the simple, robust, a posteriori scheme proposed in [29]. Let $x_\gamma,\ \gamma = 1, \ldots, p$ denote the subset of locations where the weights are negative, $\bar{\lambda}$ denote the average magnitude of the negative weights, and $\bar{C}$ denote the average covariance.

$$\bar{C} = \frac{1}{p} \sum_{\gamma=1}^{p} C_I(x_0 - x_\gamma) \tag{8}$$

between x_0 and the negative weight locations. The negative weights are set to zero. Positive weights smaller than $\bar{\lambda}$ whose covariance to the location x_0 is smaller than $\bar{C}$ are also set to zero. The remaining positive weights are renormalized uniformly to sum to one.

Indicator kriging preserves the exactitude requirement of honoring the data values at data locations, specifically

$$P(z_c; x_{\alpha'} | n) \equiv i(z_c; x_{\alpha'}) \tag{9}$$

The estimate (6) does not necessarily preserve ordering; i.e., does not preserve

$$z_{c_1} \leq z_{c_2} \Longrightarrow P(z_{c_1}; x_0 | n) \leq P(z_{c_2}; x_0 | n) \tag{10}$$

This order relation problem must be dealt with; see (21) and related discussion below.

3 Mardia-Hainsworth Spatial Thresholding

Consider an image with two populations $\Pi_i, i = 0, 1$, with associated a priori probabilities ϕ_0, ϕ_1, such that $\phi_0 + \phi_1 = 1$. Let $z(x)$ denote the gray level of any voxel x in the image. For population Π_i, assume $z(x)$ is an outcome of a stationary isotropic Gaussian process $Z(x)$, i.e.,

$$Z \sim N(\mu_i, \sigma_i), \quad \mathrm{Cov}[Z(x), Z(y)] = \sigma_i^2 \rho(|x - y|). \tag{11}$$

Here $\rho(|x - y|)$ is the spatial correlation function for $Z(x)$, which is related to the spatial covariance $C(x - y)$ of (2) by $\rho(x - y) = C(x - y)/\sigma_i^2$. As the process is assumed stationary and isotropic, $\rho(x - y) = \rho(|x - y|)$. Mardia and Hainsworth further assume local spatial continuity [30] in that, for a small neighborhood, these assumptions hold at x with high probability.

Consider an arbitrary voxel x_0 in the image. We wish to assign the observation $z(x_0)$ to one of the populations Π_i. Let $\{x_p\}, p = 1, \ldots, s$ be some neighborhood of x_0 and let $Z_p \equiv Z(x_p)$. Consider the linear combination of random variables of this neighborhood

$$G = \sum_{p=0}^{s} \gamma_p Z_p, \tag{12}$$

for respective (as yet arbitrary) weights γ_p assigned to Z_p. Then, for population Π_i, under the assumption of local spatial continuity, G is a Gaussian random field,

$$\begin{aligned} &G \sim N(\mu_i^*, \sigma_i^*), \\ &\mathrm{Cov}[G(x_p), G(x_q)] = \sigma_i^{*2} \rho(|x_p - x_q|), \end{aligned} \tag{13}$$

where

$$\begin{aligned} &\mu_i^* = \nu^2 \mu_i, \qquad \nu^2 = \sum_{p=0}^{s} \gamma_p, \\ &\sigma_i^{*2} = \beta^2 \sigma_i^2, \quad \beta^2 = \sum_{p=0}^{s} \sum_{q=0}^{s} \gamma_p \rho(|x_p - x_q|) \gamma_q. \end{aligned} \tag{14}$$

The MH method [25] assigns the observation $z(x_0)$ to that population which maximizes the score

$$S_i = \log \phi_i - \frac{1}{2} \frac{(G - \mu_i^*)^2}{\sigma_i^{*2}} - \frac{1}{2} \log(2\pi \sigma_i^{*2}). \tag{15}$$

As G is a Gaussian variable, this is equivalent to the Bayes' allocation rule which assigns an observed outcome of G to that population Π_i which maximizes the likelihood $\phi_j L_j(G)$ where $L_j(G)$ is the likelihood of G under Π_j. Thus, the value(s) G^* at which $S_0 = S_1$ provide global threshold values by which the population assignments can be determined. These results hold for any choice of the weights γ_p, however, only cases $\nu^2 > 0$ make physical sense.

MH investigate two choices for the weights. In their first choice, the weights γ_p satisfy the linear system

$$\sum_{q=0}^{s} \rho(|x_p - x_q|) \gamma_q = 1. \tag{16}$$

This choice is appropriate [31] when, instead of maximizing (15), one maximizes the modified score

$$S_i^* = \frac{\mu_i}{\sigma^2} (G - \nu^2 \mu_i / 2). \tag{17}$$

Maximizing (17) is equivalent to maximizing (15) when $\phi_0 = \phi_1 = 0.5$ and $\sigma_0 = \sigma_1 = \sigma$. Their second choice utilizes mean weighting

$$\gamma_p = 1/(s + 1) \tag{18}$$

which incorporates the spatial correlation structure only in the computation of σ_i^* and not in μ_i^*.

When prior knowledge of the statistical variables ϕ_i, μ_i, $\sigma_i, i = 0, 1$ and $\rho(|x_p - x_q|)$ for an image is unknown (the usual case), MH adopt an iterative scheme based on [26]. In each iteration, estimates for ϕ_i, μ_i, σ_i, and $\rho(|x_p - x_q|)$ are generated based on current population assignments. While the iterative method of [26] converges [32], it can generate different solutions for different initial conditions. This presumably also holds for the MH method.

4 Indicator Kriging Based Segmentation

Our kriging based segmentation algorithm is a two pass algorithm over the image. In the first pass, partial population assignment is done based upon a thresholding window. We refer to this first pass as the thresholding or a priori population assignment step. In the second pass, the remainder of the population assignment is achieved by indicator kriging; we refer to this as the kriging step.

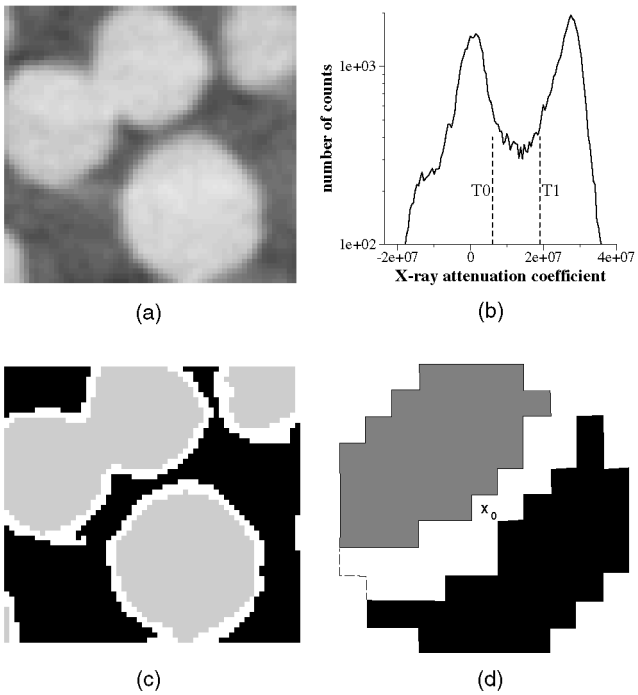

Fig. 1. (a) A portion of a CAT image of a slice of basalt imaged at 20 micron resolution. (b) The X-ray attenuation coefficient histogram for the entire sample. (c) A priori identification of the image into partial population assignments: grain (black), void (gray), unassigned (white), based upon the thresholds T_0 and T_1 shown in (b). (d) Illustration of a two dimensional kriging window used in determining the population assignment for voxel x_0.

4.1 Thresholding Step

Consider the small section of a CAT image of a slice of basalt (imaged at 20 micron resolution) shown in Fig. 1a. The histogram of the entire slice is displayed in Fig. 1b. The histogram is typical of two populations, each of a univariate process $Z(x)$ (for CAT scans the histogramed variable is the X-ray attenuation coefficient). Here, the lower peak is associated with the void phase, the upper peak with the material phase. Consider the two threshold values T_0 and T_1 indicated by the dashed lines on the histogram. (We discuss methods for choosing these threshold values below. Conceptually, these values can be chosen based upon some a priori knowledge of the image, in practice we employ methods based upon examination of the gray scale histogram of the image intensity.) The histogram region between the threshold values isolates the problematic segmentation range. As can be seen from Fig. 1c, which shows the spatial distribution of the voxels in the three X-ray coefficient ranges delineated by the two thresholds $z \leq T_0$ (colored gray in Fig. 1c), $T_0 < z < T_1$ (white), and $T_1 \leq z$ (black), most of the unidentified voxels lie on the material/void boundary. In the threshold step, the gray/black voxels are labeled as belonging, respectively, to void/material populations, the white voxels remain without population assignment.

4.2 Kriging Step

Let x_0 denote the spatial location of an unclassified voxel; let $x_\alpha, \alpha = 1, \ldots, n$ denote the spatial locations of voxels in a neighborhood of x_0. The neighborhood will be called a kriging window. A representative voxel x_0 and a digitized circular neighborhood of x_0 are illustrated in Fig. 1d. From (6), the probability $P(T_i; x_0|n) \equiv \text{Prob}\{z(x_0) \leq T_i\}$ is estimated by

$$P(T_i; x_0|n) = \sum_{\alpha=1}^{n} \lambda_\alpha(T_i; x_0) i(T_i; x_\alpha), \quad i = 0, 1. \tag{19}$$

$P(T_0; x_0|n)$ represents the probability that the unknown voxel belongs to population Π_0 and $1 - P(T_1; x_0|n)$ represents the probability it belongs to Π_1. The kriging step assigns

$$Z(x_0) \in \begin{cases} \Pi_0 & \text{if } P(T_0; x_0|n) > 1 - P(T_1; x_0|n), \\ \Pi_1 & \text{otherwise.} \end{cases} \tag{20}$$

If the kriging window is always centered on the unclassified voxel and does not change shape or size, the kriging system (7) is independent of x_0; system (7) need be solved only once and the same weights $\lambda_\alpha(T_0; x_0)$ and $\lambda_\alpha(T_1; x_0)$ are applied in calculating the probabilities $P(T_0; x_0|n)$ and $P(T_1; x_0|n)$ for all x_0. Negative weights are adjusted as discussed earlier.

The radius of the kriging window should be on the order of the correlation lengths of $C_I(T_i; \cdot)$, while still large enough to contain a sufficient number of known data points. In the 2D examples in Section 5, we used circular windows of radius 3 centered at x_0 ($n = 28$). For x_0 near the boundary of the image, the kriging window may extend beyond the boundary. To avoid recomputing (7) for a modified kriging window, we assign $i(T_0; x) = i(T_1; x) = 0.5$ for any location x in the unmodified kriging window that lies exterior to the image boundary.

We reduce the severity of the order relation problem (10) of indicator kriging utilizing the suggestion in [33] by smoothing the indicator function using the cumulative density function $F(z)$ estimated from the original data. The smoothed indicator function, $\hat{i}(T_i; x_\alpha)$ is given by

$$\hat{i}(T_i; x_\alpha) = \begin{cases} 1 & \text{if } z(x_\alpha) < T_i - s_i^l, \\ 0 & \text{if } z(x_\alpha) > T_i + s_i^r, \\ \frac{F(T_i + s_i^r) - F(z(x_\alpha))}{F(T_i + s_i^r) - F(T_i - s_i^l)} & \text{otherwise.} \end{cases} \tag{21}$$

Here, $s_0^l \equiv s_1^r \equiv 0$, and $s_0^r = s_1^l = (\sigma_0 T_1 + \sigma_1 T_0)/(\sigma_0 + \sigma_1)$ where σ_0 and σ_1 are, respectively, the standard deviations of the thresholded Π_0 and Π_1 population voxels. This smoothed indicator function is used in (19); the indicator covariances $C_I(T_0; \cdot)$ and $C_I(T_1; \cdot)$ needed in the kriging system (7) are computed directly from the indicator data $\hat{i}(T_0; \cdot)$ and $\hat{i}(T_1; \cdot)$, respectively.

Note that the original data values $z(x_\alpha)$ are used in (21) for all voxels x_α in the neighborhood of x_0 to guarantee the kriging step produces a unique result that is not dependent of the order in which the unclassified voxels are considered.

This completes the description of the basic form of the indicator kriging based segmentation. We consider now methods of choosing the T_0, T_1 values in the thresholding step. We also discuss a modification of the basic two step algorithm to further filter errors.

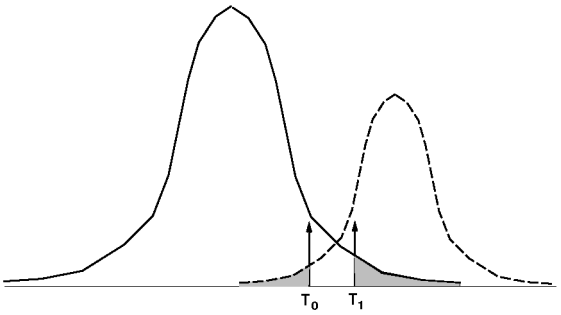

Fig. 2. Voxel misidentification under choice of T_0 and T_1.

4.3 Determination of T_0, T_1

4.3.1 Entropy Method

Applying information theory [34], Pun [6], Kapur et al. [5], and Johannsen and Bille [4] have developed segmentation methods based upon choice of a single threshold which maximize entropy functions derived from the original gray-scale distributions of the image. We use the entropy function $\psi(z)$ described in [5] to determine the thresholds T_0 and T_1. Based on the entropy maximizing value z^*, we choose the thresholds T_0 and T_1 as

$$\begin{aligned} T_0 &= \max_{z<z^*}\{z : \psi(z) = (1-r_e)\psi(z^*)\}, \\ T_1 &= \min_{z>z^*}\{z : \psi(z) = (1-r_e)\psi(z^*)\}, \end{aligned} \tag{22}$$

where $r_e \in (0,1)$. The parameter r_e is to be chosen to fit the requirements of the data. We will refer to indicator kriging segmentation using entropy based thresholding as the $\mathrm{IK_E}$ method.

4.3.2 Binormal Mixture

As a second approach, if both populations are suspected of being univariate normal, $\Pi_i \sim N(\mu_i, \sigma_i), i = 0, 1$, the histogram will have the form

$$f(z) = \sum_{i=0}^{1} \phi_i \frac{1}{\sigma_i\sqrt{2\pi}} \exp^{-(z-\mu_i)^2/(2\sigma_i^2)}, \tag{23}$$

where the populations are labeled such that $\mu_0 < \mu_1$. There are various algorithms [35] to estimate the parameters μ_i, σ_i, $i = 0, 1$ from an observed histogram; we utilize the EM algorithm [35].

Once these parameters have been estimated, consider the values

$$\begin{aligned} z_0 &= \min(\mu_0 + r_b\sigma_0, \mu_1), \\ z_1 &= \max(\mu_1 - r_b\sigma_1, \mu_0), \end{aligned} \tag{24}$$

where r_b is a positive constant to be discussed. Depending on the relative sizes of $r_b\sigma_0$ and $r_b\sigma_1$, there are two cases, either $z_0 < z_1$, in which case we define the two populations as being "well-separated" with respect to r_b, or $z_0 > z_1$, and the two populations are "poorly separated" with respect to r_b. In either case, we set the thresholds as

$$\begin{aligned} T_0 &= \min(z_0, z_1), \\ T_1 &= \max(z_0, z_1). \end{aligned} \tag{25}$$

The choice of r_b is influenced by the fraction of voxels having gray-level values $z \in [z_{\min}, T_0] \cup [T_1, z_{\max}]$ that are misclassified by the choice of T_0 and T_1. The shaded areas in Fig. 2 represent the fraction M of such voxels that are misidentified by the choice of T_0 and T_1. M is given by

$$M(r_b) = \phi_0\left[1 - \Phi\left(\frac{T_1-\mu_0}{\sigma_0}\right)\right] + \phi_1\Phi\left(\frac{T_0-\mu_1}{\sigma_1}\right), \tag{26}$$

where $\Phi(x)$ is the standardized normal cumulative density function. Analogously, the fraction R of voxels having gray level in the range $[z_{\min}, T_0] \cup [T_1, z_{\max}]$ that are correctly identified due to the choice of T_0 and T_1 is

$$R(r_b) = \phi_0\Phi\left(\frac{T_0-\mu_0}{\sigma_0}\right) + \phi_1\left[1 - \Phi\left(\frac{T_1-\mu_1}{\sigma_1}\right)\right]. \tag{27}$$

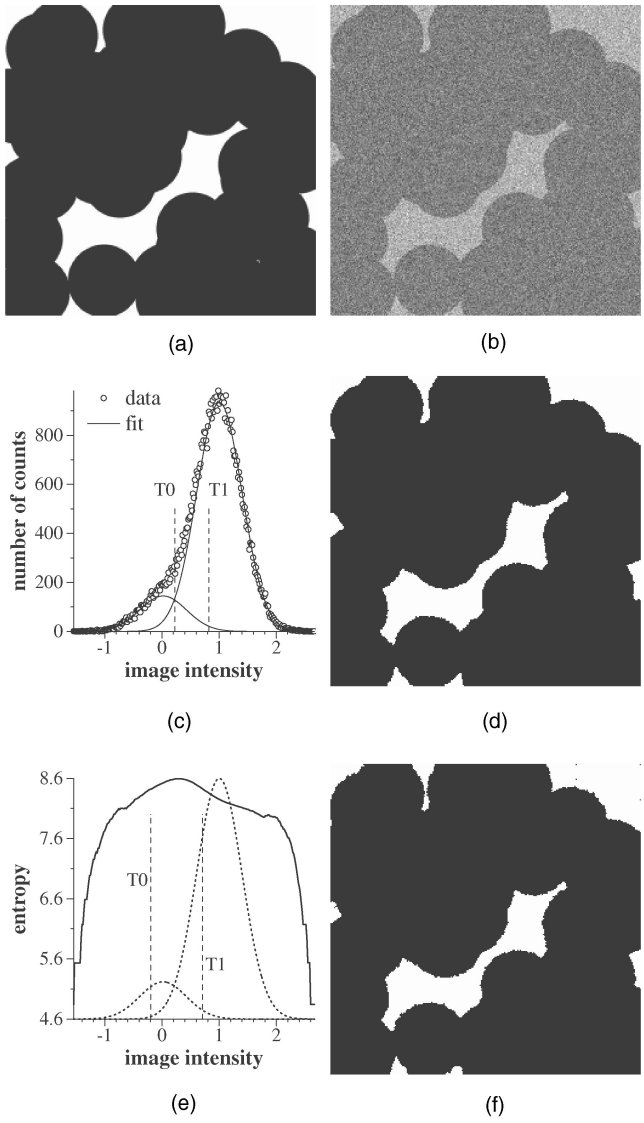

Fig. 3. Kriging based segmentation results for the synthetic data set (a). The test image (b) created by adding Gaussian noise $N(0, 0.4)$. (c) The histogram (open circles) for the test image, the binormal fit (solid line) obtained using the EM algorithm, and thresholds T_0 and T_1 obtained with $r_b = 1.96$. (d) The $\mathrm{IK_M}$ image obtained with $r_b = 1.96$ thresholds values. (e) The entropy function (solid line) for the test image showing the thresholds T_0 and T_1 obtained with $r_e = 0.02$. Superposed (dotted lines) is the histogram binormal fit. (f) The $\mathrm{IK_E}$ image obtained using $r_e = 0.02$ threshold values.

TABLE 1
Summary of the Segmentation Results for the 2D Synthetic Image

method	IK_M			IK_E			AMT-MF	global
r_b or r_e	1.0	1.96	0.0	0.005	0.01	0.02		
T_0	0.429	0.227	0.021	0.082	−0.016	−0.197	0.867	0.287
T_1	0.608	0.820	1.005	0.477	0.576	0.707		
% image kriged	8.61	29.40	49.48	11.31	17.82	28.67		
PE								
thresholding	0.0837	0.0380	0.0150	0.0303	0.0198	0.0100		0.0654
1st MF	0.0135	0.0200	0.0130	0.0159	0.0134	0.0088		0.0145
kriging	0.0097	0.0086	0.0080	0.0297	0.0284	0.0320		
final	0.0051	0.0046	0.0049	0.0089	0.0084	0.0114	0.0044	0.0145
RE								
porosity	0.0092	0.0108	0.0129	0.0562	0.0571	0.0844	0.0066	0.0938
SSA	0.1044	$1.9 \cdot 10^{-6}$	0.0194	0.1383	0.0291	0.0178	0.0324	1.044
CPU(sec)	2.56	3.49	4.84	2.12	2.43	2.99	7.24	0.42

(SSA: Specific surface area)

In a "well-separated" case we can easily show that $R(r_b) = \Phi(r_b)$ and $M(r_b) \leq 1 - \Phi(r_b)$. In a "poorly separated" case we have $M(r_b) = 1 - \Phi(r_b)$ and $R(r_b) \leq \Phi(r_b)$. In either case, $M(r_b)$ does not exceed $1 - \Phi(r_b)$. In the examples shown in Section 5, we consider the choices $r_b = 1.96$, 1.0 and 0.0 for which $M(r_b)$ cannot exceed 0.025, 0.159, and 0.5, respectively. We will refer to indicator kriging segmentation using binormal mixture based thresholding as the IK_M method.

4.3.3 User Choice

In cases where the thresholds are picked based upon other considerations, we shall refer to the resultant kriging based segmentation as IK_U.

4.4 Majority Filtering

As sketched in Fig. 2, segmentation of part of the image using the thresholds T_0 and T_1 introduces misidentification whose severity depends upon the separation $T_0 - T_1$. As the kriging step depends upon the a priori identification of the voxels from the thresholding step, it is desirable to reduce potential misidentification in the thresholding step as much as possible. Majority filtering provides a simple, but fairly effective way to remove uncorrelated isolated voxel noise, and we have included it in our general algorithm as a clean-up device *only for those voxels whose population assignment is determined by thresholding*. Thus, after the thresholding step, but before the kriging step, we implement a majority filter (MF) sweep. This MF pass involves three voxel populations, Π_0, Π_1 and unknown voxels. The unknown voxels are ignored as follows. The MF window is centered only on a threshold-assigned voxel. The population type of this voxel is changed *only* if the majority of the voxels in the MF window were threshold-assigned to be of the other known population type. For each voxel x_0 whose population type is changed to Π_0 in the filtering sweep, we reset $\hat{i}(T_0; x_0) = \hat{i}(T_1; x_0) = 1$; if changed to Π_1, we reset $\hat{i}(T_0; x_0) = \hat{i}(T_1; x_0) = 0$.

We additionally perform a second MF pass after the kriging step, again *only over voxels whose population type was determined by the thresholding step*. This second sweep affects threshold assigned voxels that lie in the neigborhood of voxels whose population assignment is done by kriging. The second MF pass is a classic two-population implementation. In both MF passes, the filtering window used is 3^2 in 2D (3^3 in 3D) and the threshold for majority is set at 60 percent.

The final indicator kriging based segmentation algorithm we consider therefore consists of four steps:

- partial population assignment by thresholding,
- majority filtering on threshold assigned voxels,
- kriging on the remainder of the voxels to complete population assignments,
- a final majority filtering sweep again over threshold assigned voxels.

The thresholding step involves two sweeps through the image, the first to compute the image histogram and the second to perform thresholding assignments. The kriging step involves three sweeps through the image, the first two compute the covariance functions $C_I(T_0; \cdot)$ and $C_I(T_1; \cdot)$, the third performing the kriging assignment based upon (19). Thus, the indicator kriging algorithm, with two majority filtering steps, involves seven passes through the data set.

5 Results

5.1 Synthetic Data

It is common to use gray-scale images (faces, buildings, industrial objects, areal photographs) and binary images (alpha-numeric characters and geometrical shapes), distorted by imaging or controlled noise, to test segmentation algorithms. Measuring the quality of segmentation of true gray-scale images requires qualitative judgement or the implementation of measures established according to human intuition concerning the "goodness" of the segmentation. Zhang [36] surveys a number of such measures. It is our preference to employ methods that quantify discrepancy between the true image and the segmented image. As our concern is ultimately the segmentation of binary images of a random geometry characterized spatially by a

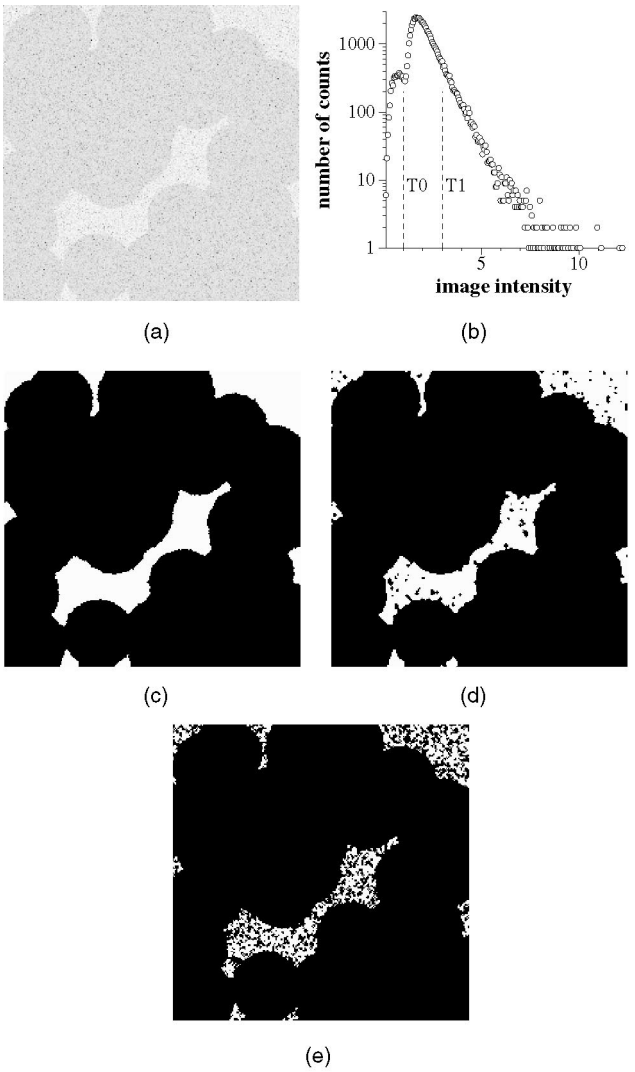

Fig. 4. Illustration of kriging based segmentation on a synthetic data set. The test image (a) is created by adding log normal noise to the true image (see Fig. 3a). (b) The histogram for the test image. The segmented images obtained from (c) kriging based segmentation with user supplied thresholds, (d) AMT-MF, (e) global thresholding.

covariance function that is stationary and isotropic (such as porous media), it is natural to consider synthetic images of geometrical objects in two- and three-dimensions. For ease of presentation we discuss 2D images here. We therefore, consider a well characterized synthetic data set obeying such statistics; a population of randomly placed, overlapping discs of constant radius.

Setting the values T_0 and T_1 determines what fraction of the image is segmented by kriging. The entropy measure and binomial fit methods use a single parameter to set both values. The usefulness of either of these "automated" means of determining the threshold values needs to be determined. Our results allow some qualitative statements to be made concerning the applicability of these two methods.

The accuracy of the segmentation by the thresholding and kriging steps must be examined as the fraction of the image determined by the kriging step is varied. Let $P(i)$ denote the a priori probability for population i in the true image. Let $P(i|j)$ denote the conditional probability that a location is assigned population i during a segmentation procedure given that the location is population j in the true image. For our two population images, we measure the accuracy of a segmentation method by computing the probability of error $PE \equiv P(0|1)P(1) + P(1|0)P(0)$. (If an image of n voxels is segmented, on average nPE will be incorrectly assigned.)

TABLE 2
Summary of the Segmentation Results for the 2D Synthetic Image With Log Normal Noise Added

method	IK_U	AMT-MF	global
T_0	1.0	2.06	1.08
T_1	3.0		
% image kriged	82.23		
PE			
thresholding	0.0295		0.0610
1st MF	0.0263		0.0567
kriging	0.0055		
final	0.0058	0.0177	0.0567
RE			
porosity	0.0034	0.1244	0.4214
SSA	0.0089	0.5930	3.3916
CPU(sec)	7.76	10.30	0.43

(SSA: Specific surface area)

We quantify the MF role by comparing the error probability sum PE for thresholding alone to PE for the same set of voxels following the first MF sweep over the image.

We are specifically interested in the ability to recover bulk image properties such as the porosity (void fraction) and material-void specific surface area (SSA) of rock images. The SSA is determined by counting voxel faces that separate the material and void phases in the segmented image and dividing by the total number of voxels in the image. As we shall see from the results, it tends to be a more sensitive measure of segmentation errors than is the porosity. We quantify discrepancy in these measurements using relative error

$$RE \equiv |true - measured|/true. \tag{28}$$

The majority of image analysis literature is concerned with 2D images. Our specific interest is in segmentation of volumetric data sets, consequently CPU time is of concern. CPU times in our results are given for an SGI Indy R5000 running with sufficient memory so that paging is not an issue.

As the MH class of methods also utilize the two-point covariance of the image, we compare our results for this test image to a method in the MH class of algorithms. Specifically, we choose the MH recommended algorithm AMT-MF of Section 5.1 in [25] which is an iterative algorithm, alternating mean weighting (18) and majority filtering each iteration. AMT-MF requires an initial threshold estimate T_0 to start the iteration. As a natural choice for T_0 for AMT-MF, we will use the mean value of the original data.

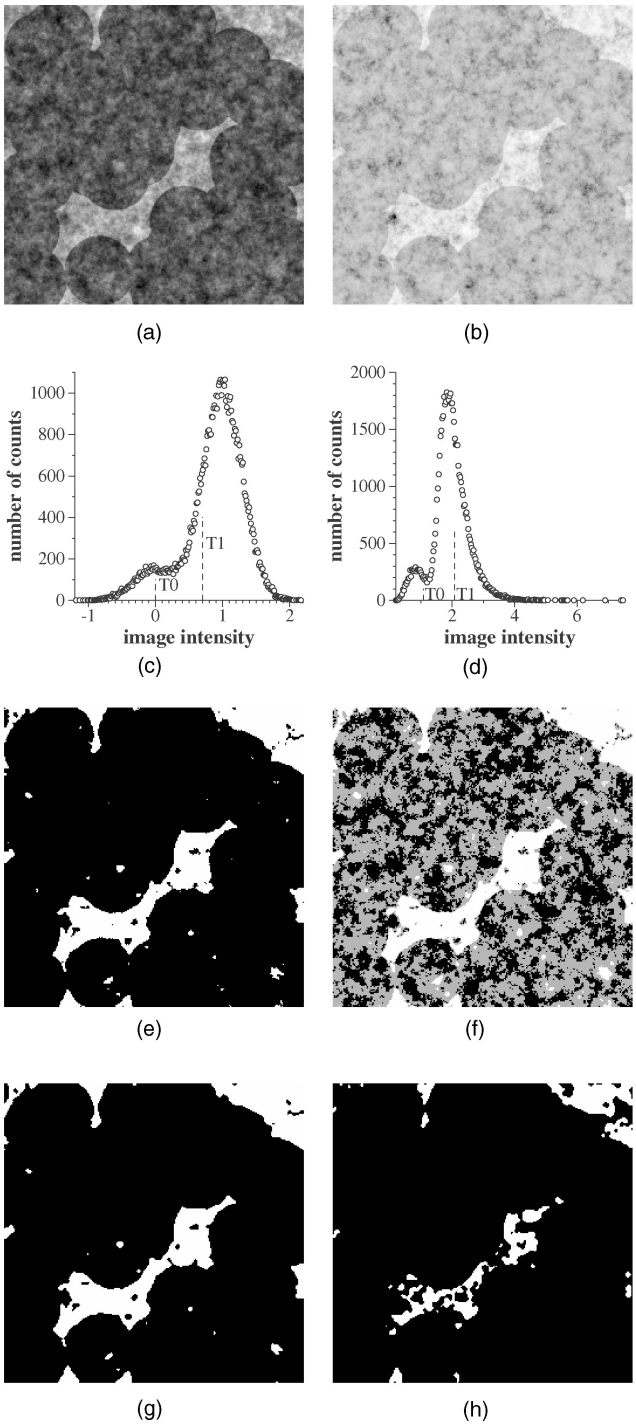

Fig. 5. Comparison of kriging based and Mardia-Hainsworth segmentation for the 2D synthetic data set with correlated Gaussian (left column) and log-normal (right column) noise. (a)-(b) Test images. (c)-(d) Histogram for each test image showing thresholds. (e)-(f) Kriging based segmentation. (g)-(h) AMT-MF segmentation.

Finally, in the synthetic images we will compare against naive global thresholding which, as mentioned earlier, is still a common method for segmenting CAT and LSCM images.

TABLE 3
Summary of the Segmentation Results for the 2D Synthetic Image With Correlated Gaussian and Log Normal Noise Added

image	Gaussian		log normal	
method	$\mathrm{IK_U}$	AMT-MF	$\mathrm{IK_U}$	AMT-MF
T_0	0.0	0.865	1.083	1.949
T_1	0.7		2.083	
% image kriged	19.6		55.3	
PE final	0.0224	0.0221	0.0318	0.07
RE				
porosity	0.07	0.09	0.026	0.52
SSA	0.69	0.38	1.09	0.44
CPU(sec)	4.55	20.73	7.11	18.69

(SSA: Specific surface area)

5.1.1 Gaussian Noise

Our 2D synthetic data set, Fig. 3a, consists of disks representing the material phase Π_1 ($z = 1$) set in a background void phase Π_0 ($z = 0$). Each disk has radius 30; their centers are randomly placed within the [0, 256] $\times$ [0, 256] square. The image is then digitized on a 256 $\times$ 256 grid. Spatially uncorrelated Gaussian noise

$$\epsilon_i(x) \sim N(0, \sigma_i), \quad i = 0, 1,$$

is then added to phase i. The test example, Fig. 3b, is generated using $\sigma_0 = \sigma_1 = 0.4$. The gray-level (image intensity) histogram (open circles) for this data is shown in Fig. 3c. As can be seen from the histogram, it is difficult to make threshold decisions for this test image. Superimposed (solid curve) is the binormal fit to the data using the EM algorithm. The EM algorithm performs well in identifying the binormal mixture in the histogram.

In $\mathrm{IK_M}$ thresholding, the parameter r_b determines the threshold values T_0, T_1. In Table 1, we show results for $r_b = 0.0$, 1.0, and 1.96, corresponding to setting the thresholds at the EM determined peak locations ($r_b = 0.0$) and at 1.0 and 1.96 standard deviations distance from the determined peak locations. For this test example, the two population peaks in the histogram are separated by only 2.5 standard deviations. As a result of (25), the choice $r_b = 1.0$ produces the smallest $T_1 - T_0$ interval.

For the three values of r_b shown in Table 1, the percentage of the image population assignment determined by kriging varies from approximately 9 to 50 percent. PE for the thresholding step shows strong sensitivity to the fraction of the image population determined by thresholding. The first MF sweep is effective in reducing PE for the thresholded voxels, largely eliminating the sensitivity of the error to the percentage of the image thresholded. In contrast to the thresholding step, PE for the kriging step shows relative insensitivity to the fraction of the image kriged. PE for the whole image is reduced even more by the second MF sweep over the thresholded population.

The porosity is relatively insensitive to changing r_b over these three values, however, the specific surface area error is very sensitive to the thresholding window choice. As expected from the algorithm, CPU times show a linear dependence on the percent of the image that is kriged.

The entropy function is shown in Fig. 3e. We investigated thresholds chosen for r_e in the range [0.005, 0.02]. Summaries for $r_e = 0.005$, 0.01 and 0.02 based segmentations are given in Table 1. The $r_e = 0.02$ threshold window is shown in Fig. 3e superimposed upon the EM binormal fit.

As the $\mathrm{IK_E}$ and $\mathrm{IK_M}$ methods differ only in threshold determinations, the results for PE for both these methods show the same trends. For the same approximate values of percentage of image kriged, the $\mathrm{IK_E}$ results for values of PE and RE are generally somewhat worse.

The AMT-MF segmentation is also summarized in Table 1. The AMT-MF segmentation of this image converged in seven iterations. In terms of error probability and porosity, the results from the AMT-MF segmentation are slightly better than indicator kriging based segmentations for this test image, although its specific surface area determination is slightly worse than four of the six indication kriging based results.

The results of naive global thresholding step at a value of $T = 0.287$ followed by a single sweep of majority filtering are also given. The thresholding step produces almost perfect porosity (which, in fact, is how this threshold value was chosen), however, at high probability of voxel misassignment. Again, the efficiency of the MF sweep in cleaning a thresholding segmentation is evident. While the naive thresholding produces a porosity correct to within 10 percent relative error, the specific surface relative error is 101 percent.

5.1.2 Log–Normal Noise

The Mardia-Hainsworth algorithm, AMT-MF, assumes the populations Π_0 and Π_1 are Gaussian. In fact a number of segmentation algorithms likewise utilize an underlying assumption of Gaussian distribution. The indicator kriging based method does not assume any specific distribution. In a second test, we compare the indicator kriging based segmentation method and AMT-MF on an image with non-Gaussian noise. Spatially uncorrelated log normal noise $\epsilon_i(x)$,

$$\log \epsilon_i(x) \sim N(0, \sigma_i), \quad i = 0, 1, \qquad \sigma_0 = \sigma_1 = 0.6,$$

is added to the synthetic image of Fig. 3a; the resultant test image is shown in Fig. 4a. The histogram of image intensities is shown in Fig. 4b. Both the Gaussian mixture and entropy methods fail to provide reasonable thresholds for this data set, instead user provided cutoffs are employed. Quantitative analysis of the results are presented in Table 2, where the indicator kriging segmentation is compared with AMT-MF and with global thresholding with the threshold chosen as the interpeak minimum. The respective segmentated images are shown in Figs. 4c, 4d, and 4e.

While AMT-MF worked well for the 2D Gaussian noise test image and poorly for the log normal noise test image, indicator kriging based segmentation works equally well for both test images.

5.1.3 Correlated Noise

Correlated noise provides a more difficult test since it introduces random structures into the image on length scales determined by the correlation length. Fig. 5a shows the test image with spatially correlated Gaussian noise

$$\epsilon_i(x) \sim N(0, 0.3), \quad i = 0, 1,$$
$$\mathrm{Cov}[\epsilon_i(x), \epsilon_i(y)] = (0.3)^2 e^{|x-y|/4},$$

added. The histogram for the image is shown in Fig. 5c; the correlation length of 4 creates structures on length scales smaller that the disk radius. The kriged image using the thresholds shown in Fig. 5c is given in Fig. 5e; the AMT-MF image is given in Fig. 5g. Figs. 5b, 5d, 5f, and 5h show the corresponding images when correlated log-normal noise

$$\log \epsilon_i(x) \sim N(0, 0.4), \quad i = 0, 1,$$
$$\mathrm{Cov}[\log \epsilon_i(x), \log \epsilon_i(y)] = (0.4)^2 e^{|x-y|/4},$$

is added. In Fig. 5f, as in all of our segmented images, the

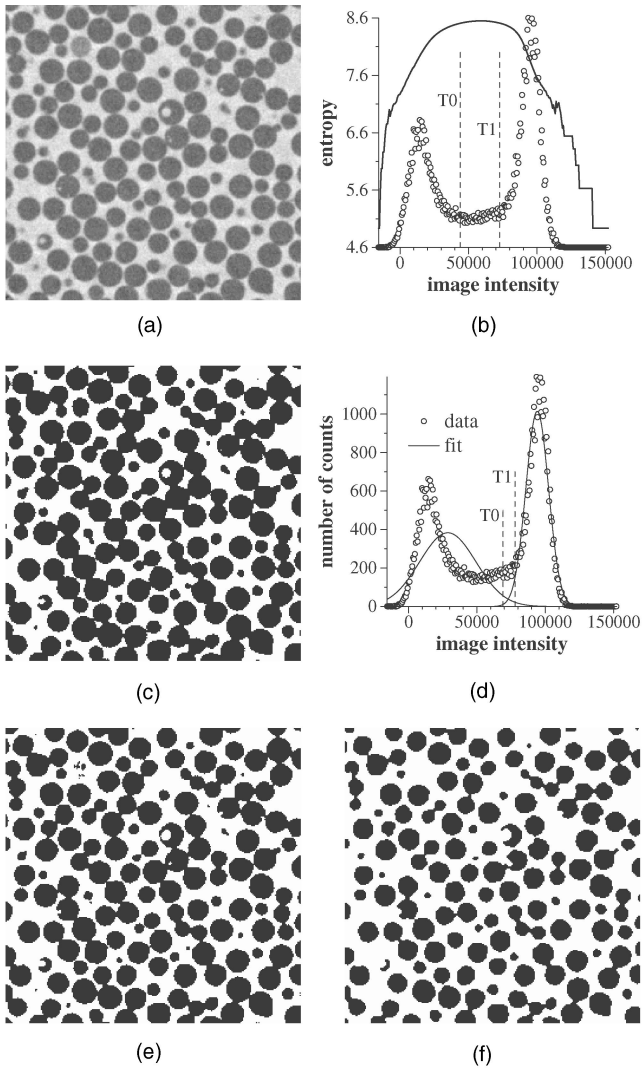

Fig. 6. Illustration of kriging based segmentation on the 100 micron diameter glass bead data set image (a). (b) The entropy function (solid line) for this image showing the thresholds T_0 and T_1 obtained with $r_e = 0.005$. The image intensity histogram (open circles) is superimposed. (c) The resultant segmented image. (d) The histogram (open circles) for the image; the binormal fit (solid line) obtained using the EM algorithm; the thresholds T_0 and T_1 obtained with $r_b = 1.96$. (e) The segmented image obtained for $r_b = 0.0$. (f) The AMT-MF segmented image.

TABLE 4
Summary of the Segmentation Results for the Three Real Images

	method	IK_E		IK_M		AMT-MF
		$r_e = 0.005$	$r_e = 0.07$	$r_b = 1.96$	$r_b = 0.0$	
Beads	T_0	43,890	15,067	69,083	28,678	62,126
	T_1	72,714	93,021	77,827	94,106	
	% image kriged	11.36	54.29	4.03	43.23	
	porosity	42.96%	41.10%	48.92%	47.46%	57.72%
	SSA	0.147	0.148	0.147	0.149	0.135
	CPU (sec)	2.05	4.93	1.89	4.12	14.43
	method	IK_U				AMT-MF
Berea	T_0	10	10			121.5
	T_1	50	100			
	% image kriged	4.79	16.41			
	porosity	20.55%	21.59%			14.51%
	SSA	0.0276	0.0291			0.0227
	CPU (sec)	7.94	11.34			105.27
	method	IK_E		IK_M		AMT-MF
		$r_e = 0.005$	$r_e = 0.05$	$r_b = 1.96$	$r_b = 0.0$	
Basalt	T_0	$-1.42 \cdot 10^6$	$-8.72 \cdot 10^6$	$3.57 \cdot 10^6$	$-6.14 \cdot 10^6$	$9.03 \cdot 10^5$
	T_1	$6.08 \cdot 10^6$	$1.60 \cdot 10^7$	$4.19 \cdot 10^6$	$1.39 \cdot 10^7$	
	% image kriged	12.63	67.84	0.74	48.55	
	porosity	60.58%	62.94%	63.27%	63.02%	62.37%
	SSA	0.060	0.061	0.063	0.061	0.057
	CPU (sec)	1.50	4.27	1.20	3.35	10.42

void phase is white, however, for this segmented image we display the material phase in two tones, black and gray. The black voxels are material voxels whose population assignment is determined by the thresholding step, gray voxels are determined during the kriging step. This figure nicely demonstrates the segmentation ability of the kriging step.

Table 3 summarizes the accuracy of the segmentations. In general, we find that the Mardia Hainsworth method is slightly better when the noise is correlated Gaussian, however, the nonparametric kriging method is much better when the correlated noise is non-Gaussian.

5.2 Real Data

We apply the kriging based segmentation method and, for comparison, the AMT-MF method to imaged samples of Berea sandstone, vesiculated basalt, and a glass bead pack. Berea sandstone is one of the two most commonly studied sandstones, having relevance to the oil reservoir industry. The pore structure of vesiculated basalts is important in volcanolgy and has relevance to contaminated waste storage. A random packing of glass beads is a classic model of rock microgeometry. Two of the samples were imaged using CAT, the third by LSCM. For simplicity of presentation, we analyze representative 2D slices from volumetric images of these samples.

5.2.1 Glass Beads—CAT Image

We consider a 250×250 voxel section of a single slice from a 3D random packing of 100 micron diameter glass beads imaged at 5 micron resolution using CAT [37]. The synthetic data sets closely approximate such a data set.

The raw image is shown in Fig. 6a. The entropy for the histogram is shown in Fig. 6b. We investigated setting thresholds using r_e in the range 0.005 to 0.07. The $r_e = 0.005$ thresholds are shown in Fig. 6b and the resultant segmented image is shown in Fig. 6c. Summary classification results for the two extremes considered, $r_e = 0.005$ and $r_e = 0.07$, are presented in Table 4.

The image histogram and binormal EM fit are shown in Fig. 6d. The upper (material) peak is well fit, the lower (void space) peak is not well fit. We investigate segmentation for r_b in the range 0.0 to 1.96. The $r_b = 1.96$ thresholds are displayed on Fig. 6d, the $r_b = 0.0$ thresholds correspond to the fitted peak maxima. Since the window determined by the $r_b = 1.96$ thresholds is extremely narrow, of the two, one would place more confidence in the $r_b = 0.0$ segmentation. The $r_b = 0.0$ segmented image is shown in Fig. 6e. The IK_M porosity results are consistently higher than the IK_E results (see Table 4). This is due to the fact that, for comparable values of T_1, the IK_M selected value for T_0 consistently lies to the right of the IK_E selected value. Ultimately this results from the poor EM fit to the void peak in the image intensity histogram.

The AMT-MF segmentation, Fig. 6f results in porosity and corresponding specific surface area values that are higher than the other segmentations.

Visual inspection of the segmentations in Fig. 6 suggests that a correct segmentation would lie somewhere between the IK_E and IK_M results. While the IK_E image has too much interbead "cementing," the IK_M results tend to miss some faint beads (see especially the sizable missing bead in the upper left hand corner of the picture). The AMT-MF result

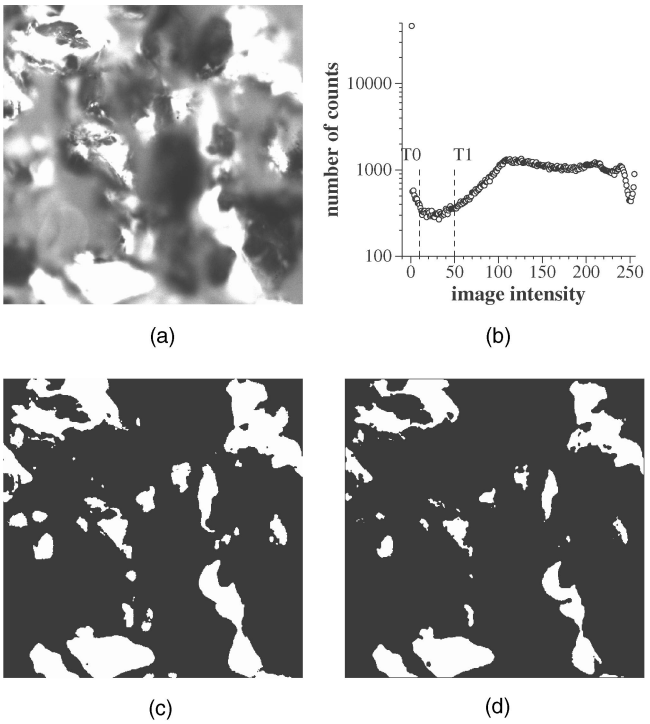

Fig. 7. Illustration of kriging based segmentation on the Berea sandstone data set (a). (b) The histogram and user selected thresholds $T_0 = 10$ and $T_1 = 50$. (c) The segmented image based upon these user selected thresholds. (d) The AMT-MF segmented image.

is clearly overestimating the porosity and underestimating the specific surface area. Note the indicator kriging segmentations run at least three times faster than the AMT-MF segmentation.

5.2.2 Berea Sandstone—LSCM Image

The second data set consists of a slice of Berea sandstone, 512×512 voxels, imaged at 1 micron resolution by LSCM [38]. The raw image is shown in Fig. 7a. As can be seen from the histogram, Fig. 7b, the image is far from a mixture of two normals. For LSCM imaging of rocks a fluorescent dye is injected into the void space. The signal from the void space is extremely narrow, in this case the majority of the void space signal occupies a single bin (bin 0 in Fig. 7b) in the reflected light intensity spectrum which was digitized into 256 bins.

The extremely well-defined void peak from this LSCM image defeats attempts to select a priori population thresholds by either the binormal mixture or entropy methods. We therefore resort to user specified thresholds. Using $T_0 = 10$ and $T_1 = 50$ to bracket the inter-peak region, the segmented image produced is shown in Fig. 7c. We also explore a wider threshold window, using $T_0 = 10$, $T_1 = 100$. As shown in Table 4, the porosities of these two segmented images agree to within 1.04 percent; their specific surface areas agree to 0.0015.

The AMT-MF segmented image is shown in Fig. 7d, visually the porosity appears underestimated. For this image, we have some numerical suggestion that the final segmented result for the AMT-MF segmentation converges to a solution that is independent of the initial threshold T_0 choice. For example if, instead of the mean value of 121.5,

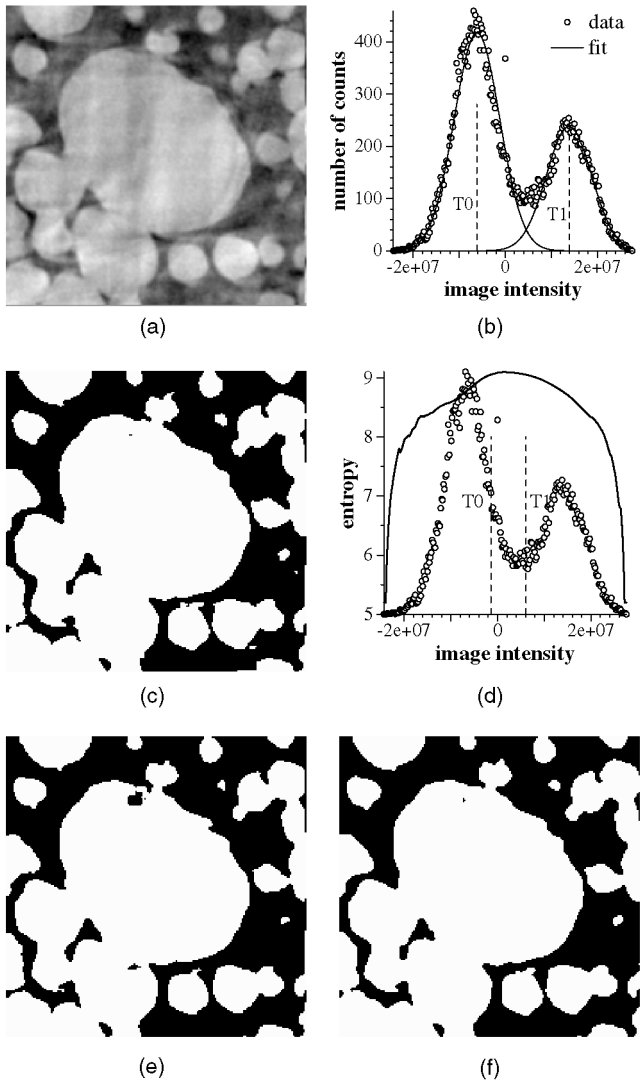

Fig. 8. Illustration of kriging based segmentation on the basalt data set (a). (b) The histogram and binormal mixture selected thresholds T_0 and T_1 for $r_b = 0.0$. (c) The segmented image based upon mixture selected thresholds. (d) The entropy function and $r_e = 0.005$ based threshold values for T_0, T_1. (e) The segmented image based upon the $r_e = 0.005$ thresholds. (f) The AMT-MF segmented image.

an initial threshold of $T_0 = 27$ is chosen, the AMT-MF algorithm converges to *exactly* the same segmented image as for the mean value choice. Note the extreme difference in CPU times between the kriged and AMT-MF segmentations for this image.

5.2.3 Vesiculated Basalt—CAT Image

The final sample is a basalt from a vesiculated lava flow imaged at 20 micron resolution by CAT. The sample is a 200×200 voxel subset of a larger slice image; the raw data is shown in Fig. 8a. The histogram, Fig. 8b (open circles), is well fit by two normally distributed populations (solid lines). The T_0 and T_1 values for $r_b = 0.0$ are shown. For these threshold values 48.55 percent of the population is kriged. The resultant segmented image is in Fig. 8c. Table 4 shows the summary of this $\mathrm{IK_M}$ segmentation as well as that for $r_b = 1.96$. Interestingly, although $r_b = 1.96$ produces an extremely narrow thresholding window resulting in only

0.74 percent of the imaged being kriged, the results are in good agreement with the $r_b = 0.0$ segmentation.

Results for thresholds picked by the entropy method with $r_e = 0.005$ and $r_e = 0.05$ are also shown in Table 4. The entropy function is shown in Fig. 8d along with the $r_e = 0.005$ threshold values. The segmented image for this threshold choice is shown in Fig. 8e. The $\mathrm{IK_E}$ segmentation with $r_e = 0.05$ is in good agreement with both the $\mathrm{IK_M}$ segmentations; the $r_e = 0.005$ segmentation results are slightly low in porosity and specific surface area.

Finally, the AMT-MF segmentation is shown in Fig. 8f and summarized in Table 4. It produces slightly lower porosity and surface area results than three of the indicator kriging threshold segmentations. The CPU time for the AMT-MF segmentation exceeds those of the indicator kriging by a factor of at least 2.5.

6 Discussion

The indicator kriging based segmentation method developed here is intended for two population, 2D and 3D images characterized by a stationary, isotropic two-point covariance function. It requires a priori partial identification of some of the image, and completes the segmentation via indicator kriging utilizing data-based estimates of the required indicator covariance functions.

We implement the a priori partial image assignment by a thresholding window on the image intensity histogram, choosing two thresholds T_0 and T_1 so that voxels having intensities below T_0 are classified as population Π_0 and above T_1 are classified as population Π_1. Choice of the threshold values controls the amount of a priori assignment misidentification error as well as the fraction of voxels whose identification is determined by the indicator kriging step.

Each of the two methods, binormal mixture and entropy function, investigated as means to automate the determination of the thresholds provide a single parameter to control threshold placements. Based upon the results displayed here and our experience, we find that the binormal mixture method tends to provide slightly better results. For either method, it is important to experiment with values for parameters r_e and r_b, in general wider threshold windows lying within the interpeak region are to be preferred. However, we have noted several cases where the interpeak threshold window can be narrowed with little change in the final results but at a savings of factors of 2 or 3 in CPU time.

For images in which non-Gaussian noise is evident, neither method may be appropriate and it is necessary to utilize human judgement in adjusting the thresholds.

In general, we find the indicator kriging based segmentations to be an improvement over the AMT-MF method of Mardia and Hainsworth, both in terms of quality of solution and in CPU time. This is especially true for images in which non-Gaussian noise is evident.

A C++ copy of the kriging based segmentation code is available from the authors by request.

Acknowledgments

This work was supported by the Geosciences program of the U.S. Department of Energy, grant DE-FG02-92ER14261 and by Sandia National Laboratories, contract AU-9640.

References

[1] N.R. Pal and S.K. Pal, "A Review on Image Segmentation Techiniques," *Pattern Recognition,* vol. 26, no. 9, pp. 1,277–1,294, 1993.

[2] H. Tek and B. B. Kimia, "Volumetric Segmentation of Medical Images by Three-Dimensional Bubbles," *Computer Vision and Image Understanding,* vol. 65, no. 2, pp. 246–258, 1997.

[3] Ø.D. Trier and A.K. Jain, "Goal-Directed Evaluation of Binarization Methods," *IEEE Trans. Pattern Analysis and Machine Intelligence,* vol. 17, no. 12, pp. 1,191–1,201, Dec. 1995.

[4] G. Johannsen and J. Bille, "A Threshold Selection Method Using Information Measures," *Proceedings, Sixth Int'l Conf. Pattern Recognition,* pp. 140–143, 1982.

[5] J.N. Kapur, P.K. Sahoo, and A.K.C. Wong, "A New Method for Gray-Level Picture Thresholding Using the Entropy of the Histogram," *Computer Vision, Graphics, Image Processing,* vol. 29, pp. 273–285, 1985.

[6] T. Pun, "A New Method for Gray-Level Picture Thresholding Using the Entropy of the Histogram," *Signal Processing,* vol. 2, no. 3, pp. 223–237, 1980.

[7] A.K.C. Wong and P.K. Sahoo, "A Gray-Level Threshold Selection Method Based on Maximum Entropy," *IEEE Trans. Systems, Man, and Cybernetics,* vol. 19, pp. 866–871, 1989.

[8] N. Otsu, "A Threshold Selection Method From Gray-Level Histograms," *IEEE Trans. Systems, Man, and Cybernetics,* vol. 9, no. 1, pp. 62–66, 1979.

[9] J.T. Tou and R.C. Gonzalez, *Pattern Recognition Principles.* Reading, Mass.: Addison-Wesley, 1974.

[10] J. Kittler and J. Illingworth, "Minimum Error Thresholding," *Patern Recognition,* vol. 19, no. 1, pp. 41–47, 1986.

[11] Y. Nakagawa and A. Rosenfeld, "Some Experiments on Variable Thresholding," *Pattern Recognition,* vol. 11, no. 3, pp. 191–204, 1989.

[12] N.R. Pal and D. Bhandari, "On Object-Background Classification," *Int'l J. Systems Science,* vol. 23, no. 11, pp. 1,903–1,920, 1992.

[13] L. O'Gorman, "Binarization and Multithresholding of Document Images Using Connectivity," *CVGIP: Graphical Models and Image Processing,* vol. 56, no. 6, pp. 494–506, 1994.

[14] A.S. Abutaleb, "Automatic Thresholding of Gray-Level Pictures Using Two-Dimensional Entropy," *Computer Vision, Graphics and Image Processing,* vol. 47, pp. 22–32, 1989.

[15] F. Deravi and S.K. Pal, "Gray Level Thresholding Using Second-Order Statistics," *Pattern Recognition Letters,* vol. 1, pp. 417–422, 1983.

[16] J.S. Weszka and A. Rosenfeld, "Threshold Evaluation Techniques," *IEEE Trans. Systems, Man, and Cybernetics,* vol. 8, pp. 622–629, 1978.

[17] T.N. Pappas, "An Adaptive Clustering Algorithm for Image Segmentation," *IEEE Trans. Signal Processing,* vol. 40, no. 4, pp. 901–914, 1992.

[18] W. Niblack, *An Introduction to Digital Image Processing.* Englewood Cliffs, N.J.: Prentice Hall, 1986.

[19] J. Bernsen, "Dynamic Thresholding of Gray-Level Images," *Proc. Eighth Int'l Conf. Pattern Recognition,* pp. 1,251–1,255, 1986.

[20] J.M. White and G.D. Rohrer, "Image Thresholding for Optical Character Recognition and Other Applications Requiring Character Image Extraction," *IBM J. Research and Development,* vol. 27, pp. 400–411, 1983.

[21] L. Eikvil, T. Taxt, and K. Moen, "A Fast Adaptive Method for Binarization of Document Images," *Proc. Int'l Conf. Document Analysis and Recognition,* Saint-Malo, France, pp. 435–443, 1991.

[22] T. Taxt, P.J. Flynn, and A.K. Jain, "Segmentation of Document Images," *IEEE Trans. Pattern Analysis and Machine Intelligence,* vol. 11, no. 12, pp. 1,322–1,329, Dec. 1989.

[23] C.K. Chos and T. Kaneko, "Automatic Detection of the Left Vectricle From Cineangiograms," *Computers and Biomedical Res.,* vol. 5, pp. 388–410, 1972.

[24] S.D. Yanowitz and A.M. Bruckstein, "A New Method for Image Segmentation," *Computer Vision Graphics, Image Processing,* vol. 46, pp. 82–95, 1989.
[25] K.V. Mardia and T.J. Hainsworth, "A Spatial Thresholding Method for Image Segmentation," *IEEE Trans. Pattern Analysis and Machine Intelligence,* vol. 10, no. 6, pp. 919–927, 1988.
[26] T.W. Ridler and S. Clavard, "Picture Thresholding Using an Iterative Selection Method," *IEEE Trans. Systems, Man, and Cybernetics,* vol. 8, pp. 630–632, 1978.
[27] A.G. Journel, *Fundamentals of Geostatistics in Five Lessons.* American Geophysical Union, 1989.
[28] A.G. Journel, "Constrained Interpolation and Soft Kriging," *Proc. 19th APCOM Symp.,* pp. 15–30, Littleton, Colo., 1986.
[29] C.V. Deutsch, "Corrections for Negative Weights in Ordinary Kriging," *Computers & Geosciences,* vol. 22, no. 7, pp. 765–773, 1995.
[30] P. Switzer, "Extensions of Linear Discriminant Analysis for Statistical Classification of Remotely Sensed Satellite Imagery," *Math. Geol.,* vol. 12, no. 4, pp. 367–376, 1980.
[31] K.V. Mardia, "Spatial Discrimination and Classification Maps," *Commun. Statist. -Theor. Meth.,* vol. 13, no. 18, pp. 2,181–2,197, 1984.
[32] F.R.D. Velasco, "Thresholding Using the Isodata Clustering Algorithm," *IEEE Trans. Systems, Man, and Cybernetics,* vol. 10, pp. 771–774, 1980.
[33] C.V. Deutsch and A.G. Journel, *GSLIB Geostatistical Software Library and User's Guide.* Oxford, England: Oxford Univ. Press, 1992.
[34] P.K. Sahoo, S. Soltani, A.K.C. Wong, and Y.C. Chen, "A Survey of Thresholding Techniques," *Computer Vision, Graphics and Image Processing,* vol. 41, pp. 233–260, 1988.
[35] D.M. Titterington, A.F. Smith, and U.E. Makov, *Statistical Analysis of Finite Mixture Distribution.* San Diego: John Wiley & Sons, 1985.
[36] Y.J. Zhang, "A Survey of Evaluation Methods for Image Segmentation," *Pattern Recognition,* vol. 29, no. 8, pp. 1,335–1,346, 1996.
[37] P. Spanne, J.F. Thovert, C.J. Jacquin, W.B. Lindquist, K.W. Jones, and P.M. Adler, "Synchrotron Computed Microtomography of Porous Media: Topology and Transports," *Phys. Rev. Letters,* vol. 73, pp. 2,001–2,004, 1994.
[38] J.T. Fredrich, B. Menendez, and T.-F. Wong, "Imaging the Pore Structure of Geomaterials," *Science,* vol. 268, pp. 276–279, 1995.

Wonho Oh received his PhD in applied mathematics from the State University of New York at Stony Brook, where he is currently a postdoctoral fellow. His research interests include geostatistics, conditional simulation, numerical solution of partial differential equations, and parallel computing.

W. Brent Lindquist received his PhD in theoretical physics from Cornell in 1981. He was a research professor at the Courant Institute, New York University until 1989 and has since been at SUNY at Stony Brook where he is a professor of applied mathematics. His research interests include numerical solution of flow in porous media where he has been a leading developer of shock-tracking methods, geostatistics at large and small length scales and its relation to fluid motion, and solutions of Riemann problems in multiple space dimensions.